Materials Advances

ROYAL SOCIETY OF CHEMISTRY

PAPER

View Article Online
View Journal | View Issue

Check for updates

Cite this: *Mater. Adv.*, 2023, 4, 2868

Received 1st April 2023,
Accepted 5th June 2023

DOI: 10.1039/d3ma00151b

rsc.li/materials-advances

Macroporous NiMo alloy self-supporting electrodes for efficient hydrogen evolution at ultrahigh current densities†

Yudan Chen,[a] Lin Chen,[b] Ying Xiong,[b] Xinxin Yu,[a] Kun Tang,*[a]
Lixin Zhang[c] and Mingzai Wu*[a]

With the aim of the rational design of industrial electrocatalysts working at high current densities over 100 mA cm^{-2} toward electrochemical water splitting, in this paper, we proposed a strategy to prepare porous arrays of NiMo alloy based hydrogen evolution reaction (HER) electrodes with high activity and good stability using the combination of the hard template method and electrodeposition technology, which showed high intrinsic activity, rapid mass transfer due to the structure of multi-scale pores and super-wetting surfaces ensuring the timely removal of evolved H_2 bubbles. The as-obtained electrodes can provide a high current density up to 500 and 1000 mA cm^{-2} at overpotentials of 306 and 491 mV, respectively in 1.0 M KOH. Our study makes it possible to design alloy HER electrodes with high activity and stability working at an industrial scale of current density and promotes the development of a hydrogen economy resulting from electrochemical water splitting.

Introduction

Presently, the energy shortage and environmental crises in the world seriously threaten the survival of humans, prompting the transformation from the conventional fossil fuel-based energy structure into a sustainable energy structure.[1] As a renewable clean energy, hydrogen exhibits no pollution and high energy density, far superior to other fossil energy sources, and has been considered as the next generation energy carrier.[2–6] The key prerequisite for hydrogen-based energy systems is to develop efficient and low-cost methods for H_2 production. However, traditional hydrogen production technologies still rely on fossil fuels with low utilization of raw materials and high pollutant emissions, causing serious harm to the environment.

Among the current accessible techniques, electrochemical reduction of water by the hydrogen evolution reaction (HER) is preferred, which shows the inherent benefits of cleanliness, durability, and higher brand purity.[6–11] Currently, the most efficient catalyst for the HER is platinum (Pt). However, its low cost-effectiveness, rarity, and limited abundance greatly restrict its use in commercial large-scale hydrogen generation.[12–18] On the other hand, for industrial applications, the current density for high-speed H_2 generation may be more than 500 or 1000 mA cm^{-2}, which calls for a high intrinsic activity for the catalyst, a wealth of active sites, rapid mass transfer of liquid electrolytes, continuous release of bubbles, and good electrochemical and mechanical stability.[19,20] Therefore, the development of base metal based electrocatalysts with high activity and good stability toward the HER working at high current density is highly demanded.

NiMo alloy has been studied and widely used for its low cost and easy production. It has good mechanical properties, stability and corrosion resistance under alkaline conditions. The element Mo is electron-deficient, while Ni is electron-rich. The alloying of Ni and Mo promotes the electron transfer and produces synergistic effects, which improves the adsorption and desorption of hydrogen, enabling it to be a promising electrocatalyst with much higher catalytic activity than that of other counterparts.[21,22] Using the template supported electrodeposition, NiMo hollow alloy nanorods arrays were reported to be endorsed on a titanium mesh with an overpotential of 310 mV in 1.0 M KOH;[23] $MoNi_4$ electrocatalysts supported by MoO_2 cuboids on foam nickel were reported to exhibit a zero initial overpotential with a low Tafel slope of 30 mV every decade and in 1 M KOH electrolyte.[24] In spite of these achievements, these

---

[a] *Key Laboratory of Structure and Functional Regulation of Hybrid Materials, Ministry of Education, Institute of Energy, Hefei Comprehensive National Science Center, Anhui University, Hefei, 230601, China. E-mail: wumz@ahu.edu.cn, tangkun0214@163.com*

[b] *School of Materials Science and Engineering, Southwest University of Science and Technology, Mianyan, China*

[c] *Department of Chemical Engineering and Environment, Shanxi Provincial Key Laboratory for High Performance Battery Materials and Devices, North University of China, Taiyuan, 030051, China*

† Electronic supplementary information (ESI) available. See DOI: **https://doi.org/10.1039/d3ma00151b**

alloy-based studies for HER catalysts were assessed at modest current densities (generally <100 mA cm^{-2}). Differently, at high current densities, the mass transfer of reactants in the electrolyte and gaseous products become increasingly rate-limited. In particular, the newly generated H_2 bubbles will severely block the catalytically active surface area, resulting in significant Ohmic resistance, thereby limiting hydrogen production efficiency and energy conversion.[25,26] Another problem associated with H_2 bubbles is that the catalyst tends to flake off due to the concentrated local stress created by bubble shedding, resulting in a decrease in activity and stability.[27–31] Thereby, the operation of the NiMo alloy HER catalyst at a high current density still presents a challenge and is not solved yet.

In this paper, we propose a strategy to prepare a self-supported electrode of NiMo alloy porous arrays on nickel foam (NiMoPA@NF) toward HER with high activity, good stability and industrial scale current density using the combination of the hard template method and electrodeposition technology, which shows unique advantages including exact composition control, porosity, and low-temperature growth. The as-obtained NiMo alloy porous electrodes exhibited the following advantages: (1) high activity (initial η-intrinsic overpotential near to zero) and low charge transfer resistance; (2) unimpeded transfer of ions and gas large due to the formation of vertically aligned pores *via* the SiO_2 temple; (3) extreme hydrophilicity and buoyancy in the presence of water, which is advantageous for the entrance of an alkaline electrolyte and the discharge of tiny-H_2 bubbles formed during electrolysis. Based on these features, the as-obtained NiMo porous arrays are allowed to function as an excellent HER electrode, delivering high current densities of 500 and 1000 mA cm^{-2} in 1 M KOH with overpotential values of 306 and 491 mV, respectively, and excellent stability, especially at high current density.

Experimental

Preparation of SiO_2 templates

In this work, the modified Stőber method was selected to prepare spherical silica with controllable particle size and good monodispersibility. Deionized water, anhydrous ethanol, 25% ammonia solution and orthosilicate (TEOS) were sequentially added into a beaker in different proportions with stirring by a magnetic stirrer for 8 h. After the reaction of the solution was completed, a series of centrifugations, washing and drying were carried out, obtaining spherical silica with a diameter of 50 nm, 100 nm, 200 nm, and 500 nm.

Preparation of NiMo PA@NF

The slice of foam nickel (1 cm × 1 cm) for the electrodeposition was treated as follows: firstly, being ultrasonically cleaned in ethanol and deionized water for 15 min to remove surface grease; secondly, being dried in a 60 °C oven for 6 h, then soaked in a 5% hydrochloric acid solution for 12 h at normal temperature to remove surface oxides; lastly, being cleaned by deionized water, and dried again at 60 °C. 24 h of being soaked in SiO_2 solution is needed for the treated nickel foam with the aid of gravity at room temperature to ensure the formation of SiO_2 sphere three-dimensional ordered arrays, which were used as a template for the electrodeposition of NiMo alloy porous arrays. NiMo electroplating solution was composed of sodium citrate (0.3 mol L^{-1}), nickel sulfate hexahydrate (0.15 mol L^{-1}), and sodium molybdate dihydrate (0, 0.02, 0.05, 0.1, 0.15 mol L^{-1}). The current density for the deposition of NiMo alloy is 25 mA cm^{-2}, and the electrodeposition time is set as 100 s, 300 s, 600 s, and 900 s, respectively. The obtained samples were immersed in 1 mol L^{-1} KOH for 24 h to remove the original SiO_2 sphere template by chemical etching. When the electrodeposition time was 900 s, the as-obtained samples using silica spheres of 50 nm, 100 nm, 200 nm and 500 nm in diameter as templates were labeled as NiMo PA-50 nm, NiMo PA-100 nm, NiMo PA-200 nm and NiMo-PA-500 nm, respectively. Similarly, when silica spheres of 200 nm in diameter were used as a template, the as-obtained samples with electrodeposition time of 100 s, 300 s, 600 s, and 900 s were labeled as NiMo PA-100s, NiMo PA-300s, NiMo PA-600s and NiMo PA-900s, respectively. When silica spheres of 200 nm in diameter were used as a template, and the electrodeposition time of 900 s was adopted, the as-obtained sample was labeled as NiMo PA@NF.

Electrochemical test

The electrocatalytic properties of the OER (oxygen evolution reaction) and HER for the prepared NiMo PA@NF were studied and analyzed in alkaline solution. A typical conventional three-electrode arrangement was used to assess the electrochemical performance at ambient temperature using the as-obtained sample as the working electrode, graphite rod as the counter electrode, saturated Ag/AgCl as the reference electrode, and 1 mol L^{-1} potassium hydroxide solution (PH = 14) as the electrolytic solution. No extra conductive binders or additives were utilized due to the self-supported nickel foam. Linear sweep voltammetry (LSV) was performed at a scan voltage of 5 mV s^{-1}.

Results and discussion

Material synthesis and characterization

SiO_2 nanospheres with a diameter of about 200 nm were evenly deposited on the surface of nickel foam, serving as a template for NiMo electrodeposition (Fig. S1a–c, ESI†). After electrodeposition of 900 s and removal of SiO_2 spheres using 1 mol L^{-1} KOH, NiMo alloy particles aggregate and form an inverted bowl-like array (Fig. 1a–c) (defined as NiMo PA). All the diffraction peaks of the NiMo alloy particles scraped off the nickel foam are indexed to the Ni_4Mo phase (JCPDS no. 65-5480). It is composed of a network of connected pores with an average diameter of about 210 nm, a little larger than the diameter of silica spheres (Fig. 2e), whose pore walls are made of many small thin intersecting nanosheets (the magnified TEM image (Fig. 2f). Well-resolved lattice fringes with an interplanar distance of 0.208 nm confirms the formation of the (121) plane of $MoNi_4$ (high resolution transmission electron microscopy image, Fig. 2g). The selected area electron diffraction (SAED)

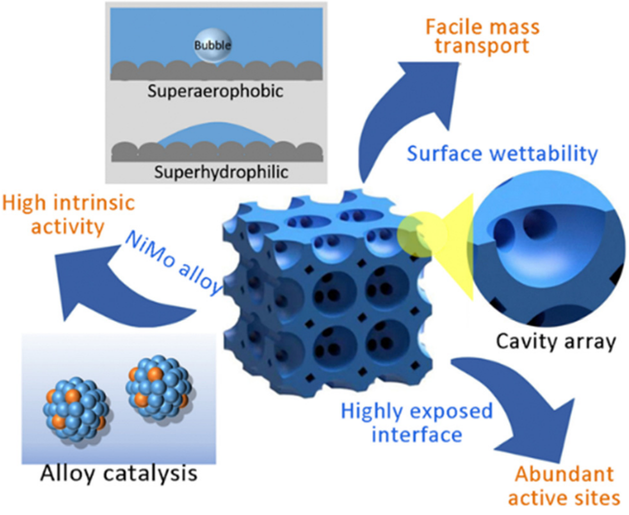

Fig. 1 The schematic diagram of the NiMo PA@NF electrode for high current density hydrogen generation, which exhibits a lot of active sites around the two-phase contact area between the catalyst and the electrolyte, hierarchical structure and super-wettability (superhydrophilic and superaerophobic), greatly boosting the mass transfer efficiency.

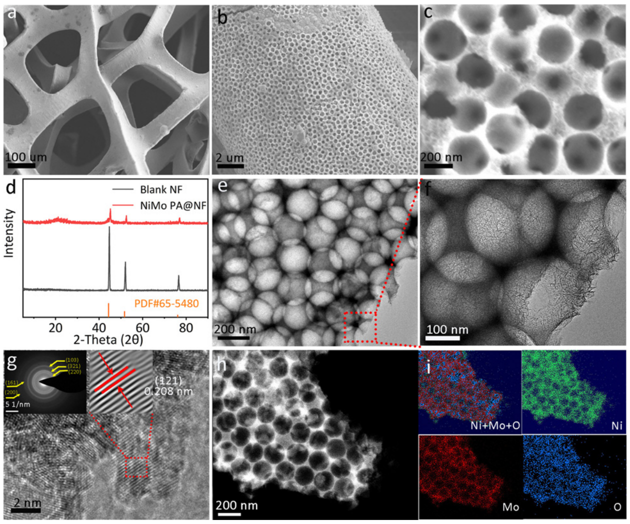

Fig. 2 (a–c) SEM images of the NiMo PA@NF; (d) XRD patterns of the NiMo alloy porous array; (e) and (f) TEM image of the NiMo alloy porous arrays; (g) HRTEM image of a NiMo alloy particle; (h) STEM image and (i) EDX element mapping images of Ni, Mo and O.

pattern (the inset in Fig. 2g) reveals the polycrystalline feature of the tetragonal $MoNi_4$.[32] No obvious morphological changes are detected between the samples with different electrochemical plating time and silica spheres with different diameters except for the pore sizes. Element mapping shows the even distribution of Ni and Mo in the porous nanoplatelets (Fig. 2i). Additionally, the EDX spectrum revealed that the atom ratio of Ni to Mo is 4 : 1 (Fig. S4, ESI†). The chemical composition and surface valence state of NiMo PA@NF were investigated by X-ray photoelectron spectroscopy (XPS), which confirms the presence of Mo, Ni, and O with a molar ratio of Mo to Ni of 1 : 4 (Fig. S5a, ESI†). Mo^0 $3d_{5/2}$ and Mo^0 $3d_{3/2}$ can be deconvolved to 227.6 and 230.8 eV, respectively, and the peaks at 852.5 and 869.7 eV belong to Ni^0 $2p_{3/2}$ and $2p_{1/2}$ (Fig. S5b and c, ESI†), which further proves the existence of Mo^0 and Ni^0 on the NiMo PA@NF surface.[33,34]

"Superaerophobic" catalyst structure

The characteristics of the solid–liquid contact interface between the catalyst and the electrolyte are crucial to the diffusion of the generated H_2 bubbles, particularly those generated at high current density, which are often locked or condensed on the catalyst surface, reducing the surface area where electrons may move between the solid and liquid. Recently, three-dimensional porous ordered nanoarrays are reported to be superhydrophilic and believed to effectively improve this issue.[35–38] For NiMo PA@NF, the measured water contact angle is nearly 0°, indicating that its surface is superhydrophilic, which allows the electrolyte to penetrate deeply into the NiMo PA@NF electrode, obtaining a highly exposed solid–liquid interface (Fig. 3a). For the sample of direct deposition of NiMo on the surface of foam nickel (defined as NiMo@NF), the measured water contact angle is about 103°, much less hydrophilic. In contrast, once the subaqueous bubble is introduced, the contact angle for NiMo PA@NF is 142°, much higher than that of NiMo@NF (110°) (Fig. 3b). Once the generated H_2 bubbles adhere to the NiMo@NF surface, they are easily immobilized, resulting in the reduction of the contact interface and the subsequent decline of the HER performance; while for the superaerophobic NiMo PA@NF, its surfaces would rapidly release the formed H_2 bubbles, keeping the original catalytic site. This is of favor to the improvement of mass transfer efficiency by promoting electrolyte entry and bubble release, and is of significance to the electrodes working at high current capability.

Electrocatalytic performance

Before the test of electrocatalytic HER activity, the optimum parameters of the electrode were investigated including the

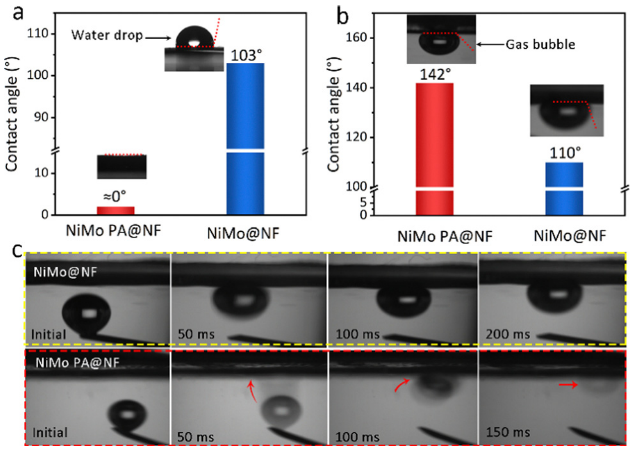

Fig. 3 Surface wettability characterization. (a) Contact angle of water droplets with NiMo@NF and NiMo PA@NF surfaces, (b) underwater bubble contact angles of NiMo PA@NF and NiMo@NF, respectively; digital images of H_2 bubbles on (c) NiMo@NF and NiMo PA@NF.

pore size and the mass loading, which can be tuned by the sizes of the silica spheres and plating time, respectively. Silica spheres with a size of 50 nm, 100 nm, 200 nm and 500 nm were chosen as the template and the corresponding as-obtained electrodes were named as NiMo PA@NF-50 nm, NiMo PA@NF-100 nm, NiMo PA@NF-200 nm and NiMo PA@NF-500 nm, respectively, which were prepared with 900 s of plating time. With the increases of the pore size from 50 nm to 200 nm, the activity and bilayer capacitance for the electrodes increase accordingly. However, the further increase of the pore size to 500 nm results in a decrease of activity (Fig. S6, ESI†). Similarly, 100 s, 300 s, 600 s and 900 s of plating time were adopted and the corresponding as-obtained electrodes were named as NiMo PA@NF-100s, NiMo PA@NF-300s, NiMo PA@NF-600s and NiMo PA@NF-900s, respectively, which were prepared using silica spheres of 200 nm as a template. With the increase of the plating time from 100 s to 900 s, the electrochemical double-layer capacitance increases. However, when the further increase of plating time is over than 900 s, the increase magnitude of the electrochemical double-layer capacitance is not as anticipated (Fig. S7, ESI†). Therefore, silica spheres with 200 nm in diameter and 900 s of plating time are chosen as the optimum parameters and the corresponding mass load was determined to be 5.8 mg cm^{-2}.

At a current density over 600 mA cm^{-2}, NiMo PA@NF exhibits better electrocatalytic activity than that of the commercial Pt/C (20 wt%) catalyst (Fig. 4a). At overpotentials of 306 and 491 mV, NiMo PA@NF can maintain current densities of 500 and 1000 mA cm^{-2}, respectively, while for commercial Pt/C catalysts, 307 mV is required to achieve a current density of 500 mA cm^{-2}, which cannot even achieve 1000 mA cm^{-2} under test conditions. Compared with NiMo@NF and blank NF, NiMo PA@NF always shows overwhelmingly better catalytic activity (Fig. 4b). The Tafel analysis was performed based on Fig. 4b and the corresponding slopes for NiMo PA@NF, NiMo@NF, Pt/C and blank NF are 107, 149, 101 and 134 mV dec^{-1}, respectively (Fig. 4c). The Nyquist diagram of electrochemical impedance spectroscopy (EIS) shows that the charge transfer resistance (R_{ct}) for NiMo PA@NF is 10.5 Ω, much smaller than that of NiMo@NF (17.2 Ω) and blank NF (89.5 Ω) at the overpotential of 100 mV, indicating that the charge transfer kinetics of the NiMo PA@NF catalyst are accelerated (Fig. S8, ESI†). To estimate the effective electrochemically active surface area of the catalyst, bilayer capacitance values are calculated. For NiMo PA@NF, the value of bilayer capacitance (6.77 mF cm^{-2}) is greater than that of NiMo@NF (2.68 mF cm^{-2}) and the blank NF (0.43 mF cm^{-2}) (Fig. S9, ESI†), suggesting more exposed active sites on the NiMo PA@NF catalyst.

The bubble release behavior of NiMo PA@NF, NiMo@NF, and Pt/C at a current density of 50 mA cm^{-2} was recorded using a high speed camera. For NiMo PA@NF, a large amount of newly generated H_2 bubbles with size less than 0.2 mm quickly escaped from the electrode (Fig. 4d and e). In contrast, H_2 bubbles are strongly immobilized on the NiMo@NF surface and coalesce into a larger size (more than 50% of the bubbles in the range of 0.2–0.5 mm) before fleeing the surface. While for the Pt/C electrode, it is hydrophobic and has a stronger adhesion of H_2 bubbles, which can grow to a size larger than 0.6 mm gradually and cannot detach from the electrode surface anymore. The difference of bubble release behavior between these electrodes can be attributed to their different surface wettability. For NiMo PA@NF, its superhydrophobic surface can timely release H_2 bubbles and re-expose its catalytic sites to the electrolyte, making it possible for the continuous generation of high throughput H_2 supply.

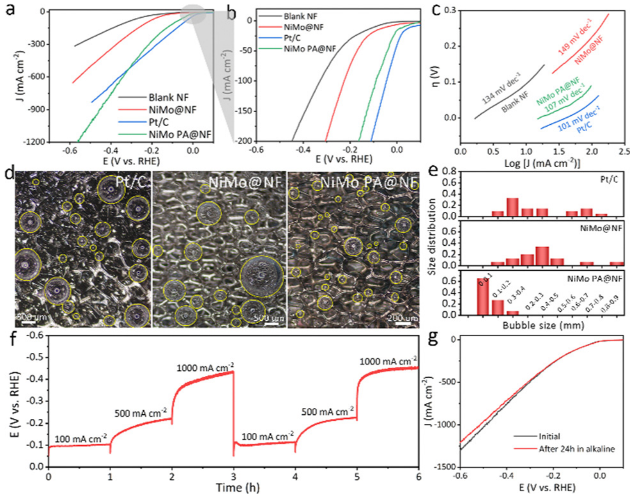

Fig. 4 Electrocatalytic performance toward the HER. (a) HER activity evaluated by linear sweep voltammetry in 1 M KOH at the scan rate of 5 mV s^{-1}; (b) enlarged part of the low overpotential region in (a); (c) Tafel slopes of different catalysts obtained from the polarization curves in (b); (d) snapshots of H_2 bubbles detached from NiMo PA@NF, NiMo@NF and Pt/C at the current density of 50 mA cm^{-2}; (e) bubble size distribution on NiMo PA@NF, NiMo@NF and Pt/C; (f) stability of NiMo PA@NF evaluated by multi-step chronopotentiometry curves at different current densities from 100 to 1000 mA cm^{-2}; (g) polarization curves of NiMo PA@NF before and after the galvanostatic stability test.

In addition to electrocatalytic activity, stability is also a key parameter for the achievement of large-scale hydrogen production. The HER stability of the NiMo PA@NF catalyst was evaluated by a variety of methods. Multi-step chronopotentiometry curves at different current densities from 100 to 1000 mA cm^{-2} show that the electrocatalytic activity remains unchanged at each step during the test (Fig. 4f). The polarization curves collected after constant current measurement almost overlap with the initial curves (Fig. 4g). In addition, the long term chronopotentiometry (500 mA cm^{-2}) test shows that the overpotentials keep almost constant with little fluctuation after 24 hours of continuous electrolysis (Fig. S10, ESI†). SEM, TEM, and XRD were used to characterize the NiMo PA@NF catalyst after the electrolytic testing. Obviously, the characteristic diffraction peak of Ni4Mo (JCPDS No. 65-5480) was clearly observed on the NiMo PA@NF catalyst after the electrolytic test (Fig. S11a, ESI†). More intuitively, the NiMo PA@NF catalyst maintained its original morphology after long term operation (Fig. S11b–d, ESI†). All of these test results support that the NiMo PA@NF catalyst exhibits excellent stability, especially at high current density. All of these test results support that the NiMo PA@NF catalyst exhibits excellent stability, especially at high current density.

Conclusions

In conclusion, the morphology of the electrodes themselves and the formation and transport of bubbles, which are affected by factors such as electrode thickness, pore spatial distribution, porosity, and pore size, constrain the conductivity and catalytic activity of the NiMo PA@NF catalyst at high current densities. The NiMo PA@NF catalyst was synthesized by electrodeposition by means of using an opal template, which was constructed by self-assembled silica nanospheres. The template method was used to alter the morphology and composition of the electrodes to establish a porous structure, optimizing the time parameters of electrodeposition and template pore sizes to expose more active sites in order to improve the hydrogen binding energy of the catalyst. The three-dimensionally ordered macroporous (3DOM) NiMo film alloy catalysts with reasonable pore size distribution, excellent morphology and high HER catalytic activity supported on nickel foam can be prepared in the electrodeposition system. In 1 M KOH alkaline solution, the catalysts have excellent electrical conductivity and electrocatalytic performance. NiMo PA@NF as a HER electrode can provide high current density up to 500 and 1000 mA cm^{-2} at overpotentials of 306 and 491 mV, respectively in 1 M KOH. The improvement in electrocatalytic performance can be attributed to the following characteristics: (1) a reasonable electrode film thickness can reduce the Ohm value on the premise of ensuring the conductivity of the electrode. (2) The introduction of a 3D ordered porous structure enhanced the gas–liquid transport capacity, facilitated the release of internal bubbles and avoided the loss of active sites due to bubble trapping at high current densities. (3) NiMo PA@NF's superhydrophilicity ensures electrolytic water infiltration, achieving a highly exposed solid–liquid contact interface at high current density. This project optimizes the existing electrode catalytic structure, thus providing a potential solution for large-scale electrolytic water industrial applications.

Author contributions

Y. C. conducted the experiment, C. Y. and K. T. conceptualized the experiment. L. C. and Y. X. carried out TEM measurement and related data analysis. X. Y. and L. Z. explained these results. K. T. and M. W. wrote the manuscript. Y. C., L. C., Y. X., X. Y. and L. Z. reviewed and edited the manuscript.

Conflicts of interest

There are no conflicts to declare.

Acknowledgements

This work was financed by the National Natural Science Foundation of China (U2003132), the Open fund projects from the South-west University of Science and Technology (21kfhg11), and the Opening Foundation of Shanxi Provincial Key Laboratory for High Performance Battery Materials and Devices (2022HPBMD01001).

References

1 L. Barreto, A. Makihira and K. Riahi, *Int. J. Hydrogen Energy*, 2003, **28**, 267–284.
2 K. Mazloomi and C. Gomes, *Renewable Sustainable Energy Rev.*, 2012, **16**, 3024–3033.
3 K. T. Møller, T. R. Jensen, E. Akiba and H.-W. Li, *Prog. Nat. Sci.: Mater. Int.*, 2017, **27**, 34–40.
4 I. Staffell, D. Scamman, A. Velazquez Abad, P. Balcombe, P. E. Dodds, P. Ekins, N. Shah and K. R. Ward, *Energy Environ. Sci.*, 2019, **12**, 463–491.
5 X. F. Lu, L. Yu and X. W. Lou, *Sci. Adv.*, **5**, eaav6009.
6 X. F. Lu, L. Yu, J. Zhang and X. W. Lou, *Adv. Mater.*, 2019, **31**, 1900699.
7 X. Shang, B. Dong, Y.-M. Chai and C.-G. Liu, *Sci. Bull.*, 2018, **63**, 853–876.
8 K.-L. Yan, J.-F. Qin, Z.-Z. Liu, B. Dong, J.-Q. Chi, W.-K. Gao, J.-H. Lin, Y.-M. Chai and C.-G. Liu, *Chem. Eng. J.*, 2018, **334**, 922–931.
9 Z. Zhang, L. Cong, Z. Yu, L. Qu, M. Qian and W. Huang, *Mater. Adv.*, 2020, **1**, 54–60.
10 J. Park, H. Kim, G. H. Han, J. Kim, S. J. Yoo, H.-J. Kim and S. H. Ahn, *J. Mater. Chem. A*, 2021, **9**, 3677–3684.
11 J.-Q. Chi, J.-Y. Xie, W.-W. Zhang, B. Dong, J.-F. Qin, X.-Y. Zhang, J.-H. Lin, Y.-M. Chai and C.-G. Liu, *ACS Appl. Mater. Interfaces*, 2019, **11**, 4047–4056.
12 B. Dong, Y.-N. Zhou, J.-C. Zhou, Y. Ma, N. Yu, R.-N. Luan, Y.-W. Dong and Y.-M. Chai, *Fuel*, 2022, **324**, 124343.
13 Y. Yan, B. Y. Xia, B. Zhao and X. Wang, *J. Mater. Chem. A*, 2016, **4**, 17587–17603.
14 Y. Zheng, Y. Jiao, Y. Zhu, L. H. Li, Y. Han, Y. Chen, A. Du, M. Jaroniec and S. Z. Qiao, *Nat. Commun.*, 2014, **5**, 3783.
15 H. Fei, J. Dong, M. J. Arellano-Jiménez, G. Ye, N. Dong Kim, E. L. G. Samuel, Z. Peng, Z. Zhu, F. Qin, J. Bao, M. J. Yacaman, P. M. Ajayan, D. Chen and J. M. Tour, *Nat. Commun.*, 2015, **6**, 8668.
16 N. Cheng, S. Stambula, D. Wang, M. N. Banis, J. Liu, A. Riese, B. Xiao, R. Li, T.-K. Sham, L.-M. Liu, G. A. Botton and X. Sun, *Nat. Commun.*, 2016, **7**, 13638.
17 J. Wei, M. Zhou, A. Long, Y. Xue, H. Liao, C. Wei and Z. J. Xu, *Nano-Micro Lett.*, 2018, **10**, 75.
18 D. Strmcnik, P. P. Lopes, B. Genorio, V. R. Stamenkovic and N. M. Markovic, *Nano Energy*, 2016, **29**, 29–36.
19 C.-T. Dinh, A. Jain, F. P. G. de Arquer, P. De Luna, J. Li, N. Wang, X. Zheng, J. Cai, B. Z. Gregory, O. Voznyy, B. Zhang, M. Liu, D. Sinton, E. J. Crumlin and E. H. Sargent, *Nat. Energy*, 2019, **4**, 107–114.
20 G. Zhang, K. Ming, J. Kang, Q. Huang, Z. Zhang, X. Zheng and X. Bi, *Electrochim. Acta*, 2018, **279**, 19–23.
21 S. Shetty, M. Mohamed Jaffer Sadiq, D. K. Bhat and A. C. Hegde, *J. Electroanal. Chem.*, 2017, **796**, 57–65.
22 W. Yuan, Z. Cui, S. Zhu, Z. Li, S. Wu and Y. Liang, *Electrochim. Acta*, 2021, **365**, 137366.
23 J. Tian, N. Cheng, Q. Liu, X. Sun, Y. He and A. M. Asiri, *J. Mater. Chem. A*, 2015, **3**, 20056–20059.

24 J. Zhang, T. Wang, P. Liu, Z. Liao, S. Liu, X. Zhuang, M. Chen, E. Zschech and X. Feng, *Nat. Commun.*, 2017, **8**, 15437.

25 X. Zhao, H. Ren and L. Luo, *Langmuir*, 2019, **35**, 5392–5408.

26 J. Yang, A. R. Mohmad, Y. Wang, R. Fullon, X. Song, F. Zhao, I. Bozkurt, M. Augustin, E. J. G. Santos, H. S. Shin, W. Zhang, D. Voiry, H. Y. Jeong and M. Chhowalla, *Nat. Mater.*, 2019, **18**, 1309–1314.

27 Q. Song, Z. Xue, C. Liu, X. Qiao, L. Liu, C. Huang, K. Liu, X. Li, Z. Lu and T. Wang, *J. Am. Chem. Soc.*, 2020, **142**, 1857–1863.

28 M. Wang, Z. Wang, X. Yu and Z. Guo, *Int. J. Hydrogen Energy*, 2015, **40**, 2173–2181.

29 L. Yu, Q. Zhu, S. Song, B. McElhenny, D. Wang, C. Wu, Z. Qin, J. Bao, Y. Yu, S. Chen and Z. Ren, *Nat. Commun.*, 2019, **10**, 5106.

30 F.-H. Yuan, M.-R. Mohammadi, L.-L. Ma, Z.-D. Cui, S.-L. Zhu, Z.-Y. Li, S.-L. Wu, H. Jiang and Y.-Q. Liang, *Rare Met.*, 2022, **41**, 2624–2632.

31 N. V. Krstajić, V. D. Jović, L. Gajić-Krstajić, B. M. Jović, A. L. Antozzi and G. N. Martelli, *Int. J. Hydrogen Energy*, 2008, **33**, 3676–3687.

32 Y. Duan, Z.-Y. Yu, L. Yang, L.-R. Zheng, C.-T. Zhang, X.-T. Yang, F.-Y. Gao, X.-L. Zhang, X. Yu, R. Liu, H.-H. Ding, C. Gu, X.-S. Zheng, L. Shi, J. Jiang, J.-F. Zhu, M.-R. Gao and S.-H. Yu, *Nat. Commun.*, 2020, **11**, 4789.

33 L. An, X. Zang, L. Ma, J. Guo, Q. Liu and X. Zhang, *Appl. Surf. Sci.*, 2020, **504**, 144390.

34 Y. Jin, X. Yue, C. Shu, S. Huang and P. K. Shen, *J. Mater. Chem. A*, 2017, **5**, 2508–2513.

35 X. Chen, L. Sheng, S. Li, Y. Cui, T. Lin, X. Que, Z. Du, Z. Zhang, J. Peng, H. Ma, J. Li, J. Qiu and M. Zhai, *Chem. Eng. J.*, 2021, **426**, 131029.

36 X. Yu, Z.-Y. Yu, X.-L. Zhang, Y.-R. Zheng, Y. Duan, Q. Gao, R. Wu, B. Sun, M.-R. Gao, G. Wang and S.-H. Yu, *J. Am. Chem. Soc.*, 2019, **141**, 7537–7543.

37 J. Zhang, X. Song, L. Kang, J. Zhu, L. Liu, Q. Zhang, D. J. L. Brett, P. R. Shearing, L. Mai, I. P. Parkin and G. He, *Chem. Catal.*, 2022, **2**, 3254–3270.

38 R. Liu, Z. Gong, J. Liu, J. Dong, J. Liao, H. Liu, H. Huang, J. Liu, M. Yan, K. Huang, H. Gong, J. Zhu, C. Cui, G. Ye and H. Fei, *Adv. Mater.*, 2021, **33**, 2103533.